

Fluid-induced vibration deformation of a nozzle flowmeter with flowrate and temperature effect

Xu-Lai Chen¹, Di Yu¹, Ji-Wei Shen², Bo Wang², He-Chao Guo², Fu-Yi Zhang²

¹ Zhejiang Testing & Inspection Institute for Mechanical and Electrical Products Quality Co., Ltd., Hangzhou, 311305, China

² College of Mechanical Engineering, Quzhou University, Quzhou, 324000, China

ABSTRACT

This article performs fluid-structure coupling numerical calculations on the internal flow field and fluid-induced vibration deformation of a nozzle flow meter under different flow conditions. It was found that at different inner wall temperatures, the internal heat transfer of a nozzle flowmeter gradually weakens with an increase in flow rate, while changes in the inner wall surface temperature have a relatively small effect on internal pressure fields, dynamic stresses, and vibration deformation caused by fluid in the flow meter.

Keywords: nozzle flowmeter, fluid-solid coupling, flow rate, wall temperature, vibration deformation

Date of Submission: 28-04-2024

Date of acceptance: 06-05-2024

I. Introduction

Accurate measurement of steam plays an important role in industrial production. Accurate and non-destructive metering of steam is important for energy saving and economic efficiency. In recent years, many scholars have conducted extensive research on the internal flow and external characteristics of various steam flow meters. Nasiruddin et al. investigated the effects of Reynolds number and boundary layer thickness on the performance of a V-cone flowmeter through CFD simulation[1]. Nasiruddin et al. discovered that introducing a curved surface at the bottom of the cone can improve the performance of a V-cone flowmeter[2]. Perumal and Jagannathan studied the effects of diameter, diameter ratio, and convergence angle on the performance of Venturi meters in measuring humid air by CFD modeling of high-pressure wet air flow[3]. Enz studied the effect of asymmetric actuator and detector position on Coriolis flowmeter and measured phase shift[4]. Huang et al. studied the characteristics of outward vibration transmission caused by wall-mounted state in a Coriolis flowmeter through harmonic response analysis[5]. Costa et al. developed a model that explains how Coriolis meters need to be corrected for temperature effects from room temperature down to cryogenic temperatures[6]. Shavrina et al. found that the increase in the gas volume fraction and the reduction in the mixture flow rate lead to the increase in the gas distribution asymmetry. The strong correlation between the gas distribution asymmetry and the experimentally observed CFM error is demonstrated[7]. Prabu et al. investigated the impact of different upstream pipe fittings on the performance of conical flowmeters and orifice flowmeters through experiments, and found that the conical flowmeter has lower sensitivity to turbulence and an irrecoverable pressure drop 50% smaller than that of the orifice flowmeter[8]. Singh et al. found that the pressure loss in the multihole orifice flow meter is significantly lower than that of single-hole orifice flow meter of identical flow area due to the early reattachment of flow in the case of the multi-hole orifice meter[9]. Morteza found that the improved hole design has a shorter length of turbulent zone and lower sensitivity to upstream disturbances by numerically simulating the flow rates through the holes of both standard and improved porous plate flowmeters[10]. Rzasa et al. conducted a numerical study on the effect of changes in vortex shedding around the surface of a body on the parameters of the von Kármán vortex street using a proprietary method to determine local liquid velocities and local vortex visualization[11]. Mohadikar et al. improved the operable range of the vortex flowmeter and enhanced its anti-interference ability by introducing an optimized contraction cone upstream of the flowmeter[12]. Guo et al. studied the effect of different blade shapes on the measurement performance of the turbine flow meter using CFD simulation[13]. Guo. et al. discovered that viscosity affects the pressure distribution on the rotor blades, which in turn affects the performance of the turbine flowmeter[14]. Zhang et al. studied the metrological performance and internal unsteady flow of a swirlmeter assembled with three swirlers with different helix angles through physical experiments and numerical calculations. The results indicate that a larger helix angle can significantly reduce the pressure and flow losses of the swirlmeter[15–16]. Chen et al. investigated the internal flow characteristics and the influence of the tube structure (geometric parameter of flow passage) on metrological performance were studied, with a

particular focus on the meter factor. Calibration experiments were performed to validate the CFD predictions; the results show good agreement with those from simulations[17]. By analyzing the relationship between Reynolds number and discharge coefficient of differential pressure flowmeters, Hollingshead et al. found that the discharge coefficients of Venturi tube, V-cone, and wedge flow meters decrease rapidly with the decrease of Reynolds number[18]. Düz conducted numerical studies on the effect of cone angle on the hydraulic characteristics of a conical inlet orifice plate and found that a 30-degree cone angle is the optimal angle with the minimum pressure loss, which enhances the performance by 13-22% compared to the commonly used 45-degree cone angle[19]. Zhang et al. proposed a correction factor for theoretical flowrate considering the real velocity profile were proposed for laminar and turbulent flow, obtaining a higher accuracy[20]. Alaeddin et al. study the effect of circumferential position of transducers on calibration factor for special type of ultrasonic flowmeters, UCCF, at different Reynolds numbers and various locations of flowmeter for the first time, and the effects of Reynolds numbers and the flowmeter distances from the elbow on the calibration factor were analyzed[21].

The orifice plate flowmeter is one of the most widely used steam flowmeters, but its drawbacks include low measurement accuracy and small measurement range[22]. The nozzle flowmeter can overcome the problems associated with standard orifice plate flowmeters in measurement. Therefore, it has been increasingly used in practical applications[23]. Oh et al. proposed a new type of multi-nozzle air flow meter, which has the advantages of small size, simple operation, and low measurement error[24]. Wang et al. achieved the optimization of the pressure tapping position by numerical simulation of a 65 mm nozzle flowmeter[25]. Zhang et al. studied the influence of wall temperature on thermal effect of nozzle flowmeter, found that with the increase of the wall temperature with, the thermal stress in the upstream and downstream pressure inlets and the inlet and outlet areas of the flowmeter increases. There are large thermal deformation areas in the inlet and outlet areas of the upstream and downstream pressure inlets and the eight-slot nozzle[26]. Kim et al. studied the pressure losses of nozzle under different fouling states and the effects on pressure losses according to fouling states by inserting a ring into the nozzle, it is found that the inserted ring reduces the fouling effect due to the flow separation occurring at the ring[27]. Zhang et al. found that there is a significant temperature stratification near the inner wall when the small-sized nozzle flowmeter is used to transport high-temperature medium, and the thermal flow field at the inlet and outlet of the flowmeter will increase accordingly with the temperature increases[28]. In recent years, CFD has been widely used for flow prediction and performance simulation of various flow meters due to its efficiency and accuracy[29].

However, there is very limited research on the thermal effects of fluid-structure coupling in nozzle flow meters. In previous published paper[30], the temperature field distribution characteristics in fluid domain has been deeply studied when the delivered medium temperature are respectively 50 °C and 700 °C. These two values are respectively the minimum temperature and the maximum temperature. Meanwhile, the pressure field distribution, dynamic stress distribution and deformation distribution of flow meter have also been deeply studied when the delivered flow rates are respectively 10 m³/h and 1000 m³/h. Similarly, these two values are also respectively the minimum flow rate and the maximum flow rate. Through these researches, some characteristics has been deeply revealed. However, the characteristics between 50 °C and 700 °C has not been revealed. Meanwhile, the characteristics between 10 m³/h and 1000 m³/h has not also been revealed. Therefore, the present paper would deeply study and reveal these characteristics. Based on this, this paper takes a nozzle flow meter as the research object, based on the unidirectional fluid-structure coupling numerical simulation method to carry out numerical calculations under different flow rates and internal wall temperature scenarios, revealing the flow field characteristics and fluid excitation deformation characteristics of the nozzle flow meter under different working conditions.

II. Calculating Model And Method

2.1 Physical model

The main structure of the nozzle flowmeter in this article consists of four parts: front measuring tube, rear measuring tube, nozzle and weld metal, and the physical structure. Material composition and calculation grid are exactly the same as in the literature[30]. Figure 1 (a) and (b) show the solid structure domain and the fluid domain calculation domain of this nozzle flowmeter respectively. Figure 2 shows the computational grid for the solid structure domain of this nozzle flowmeter.

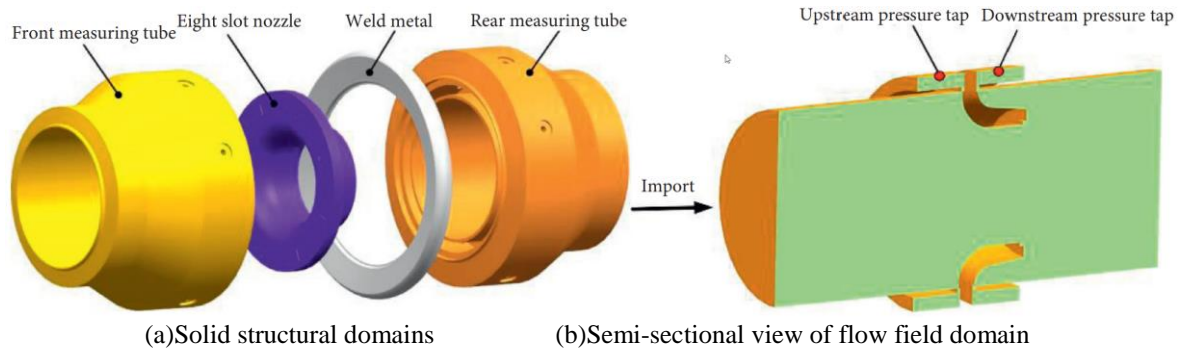


Figure 1 Computational Domain

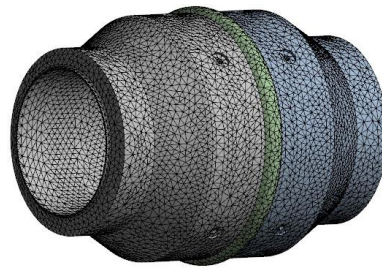


Figure 2 Grid of solid field structured domains

2.2 Solving equations

The computational fluid dynamics software FLUENT is used to calculate the flow field inside the flowmeter. The solid field is simulated numerically using the finite element analysis software ANSYS Work-bench. The numerical calculation of three-dimensional steady state viscous flow is carried out using the standard $k-\varepsilon$ turbulence model. Assuming that an incompressible fluid is used in the nozzle flowmeter, the equations for the turbulent dissipation rate ε and turbulent kinetic energy k in the standard turbulence model are:

$$\rho \frac{Dk}{dt} = \frac{\partial}{\partial x_i} \left[\left(\mu + \frac{\mu_t}{\sigma_k} \right) \frac{\delta k}{\delta x_i} \right] + P_k - \rho \varepsilon \quad (1)$$

$$\rho \frac{D\varepsilon}{dt} = \frac{\partial}{\partial x_i} \left[\left(\mu + \frac{\mu_t}{\sigma_\varepsilon} \right) \frac{\partial \varepsilon}{\partial x_i} \right] + \frac{\varepsilon}{k} C_{\varepsilon 1} P_k - C_{\varepsilon 2}^* \rho \frac{\varepsilon^2}{k} \quad (2)$$

In the equation: P_k is the generating term for turbulent kinetic energy. k and ε have the following expressions:

$$P_k = -\overline{\rho u' u'_j} \frac{\partial u_j}{\partial x_i} \quad (3)$$

$$k = \frac{1}{2} \overline{u' u'_i} \quad (4)$$

$$\varepsilon = \nu \frac{\overline{\partial u'_i \partial u'_i}}{\partial x_j \partial x_j} \quad (5)$$

Turbulent viscosity is calculated from k and ε and is given by:

$$\mu_t = C_\mu \rho \frac{k^2}{\varepsilon} \quad (6)$$

C_μ is a constant in the formula. From experience, $C_{\varepsilon 1}=1.44$, $C_{\varepsilon 2}^*=1.92$, $C_\mu=0.99$, $\sigma_k=1.0$, $\sigma_\varepsilon=1.3$.

In this study, a one way fluid solid coupling method is employed for fluid solid coupling calculations, as the deformation of the nozzle flowmeter structure under fluid forces is relatively small. The SIMPLEC algorithm is used to to achieve the coupling calculation between velocity and pressure. The measuring medium inside the nozzle flowmeter is ordinary air, which is considered as an incompressible fluid in this pape. The boundary conditions of all solid walls are set as the standard wall boundary conditions, among which the setting for the stationary wall is a smooth wall with a standard wall function in the near-wall region. The spatial discretization for the convective term is implemented using a second-order upwind scheme, while the spatial discretization for the diffusive term is accomplished using a centered differencing scheme.

III. Result analysis

3.1 Temperature field

In this study, the outer wall temperature was uniformly set at 20°C and kept constant throughout the calculations. Figure 3 shows the cross-sectional temperature distribution of the fluid domain at various flow rates when the inner wall temperature is set to 100°C. As the flow rate increases, the internal heat transfer inside the nozzle flowmeter gradually decreases. During the process of increasing the flow rate from 10m³/h to 1000m³/h, the temperature stratification phenomenon in the internal temperature field of the flowmeter weakens. When the flow rate is 10m³/h, the heat transfer in the internal fluid domain of the nozzle flowmeter is more pronounced. There is a smaller area of low-temperature region inside, and the high-temperature region extends towards the outlet of the flowmeter. When the flow rate is 1000m³/h, the heat transfer phenomenon inside the nozzle flowmeter is weaker, and the internal temperature stratification is mainly concentrated in the low temperature section.

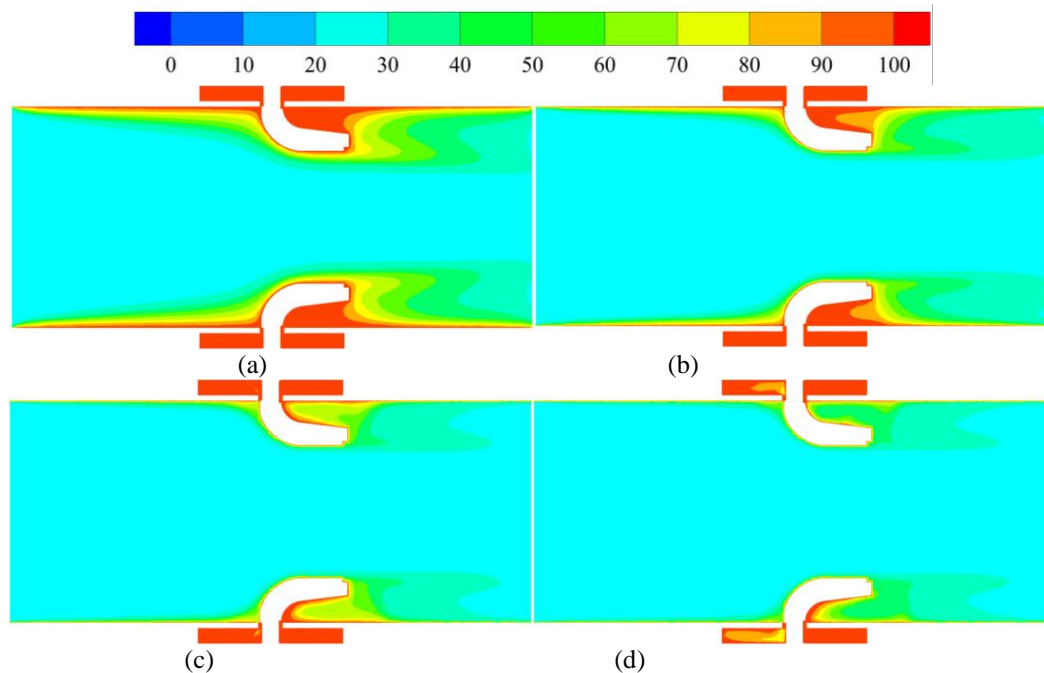


Figure 3 Temperature field of the cross-section in the flowmeter at 100°C
(a)10m³/h (b)100m³/h (c)500m³/h (d)1000m³/h

Figure 4 shows the cross-sectional temperature distribution of the fluid domain at various flow rates when the inner wall temperature is set to 300°C. As the flow rate increases, the internal heat transfer inside the nozzle flowmeter gradually decreases. During the process of increasing the flow rate from 10m³/h to 1000m³/h, the temperature stratification phenomenon in the internal temperature field of the flowmeter weakens. When the flow rate is 10m³/h, the heat transfer in the internal fluid domain of the nozzle flowmeter is more pronounced. There is a smaller area of low-temperature region inside, and the high-temperature region extends towards the outlet of the flowmeter. When the flow rate is 1000m³/h, the heat transfer phenomenon inside the nozzle flowmeter is weaker, and the internal temperature stratification is mainly concentrated in the low temperature section.

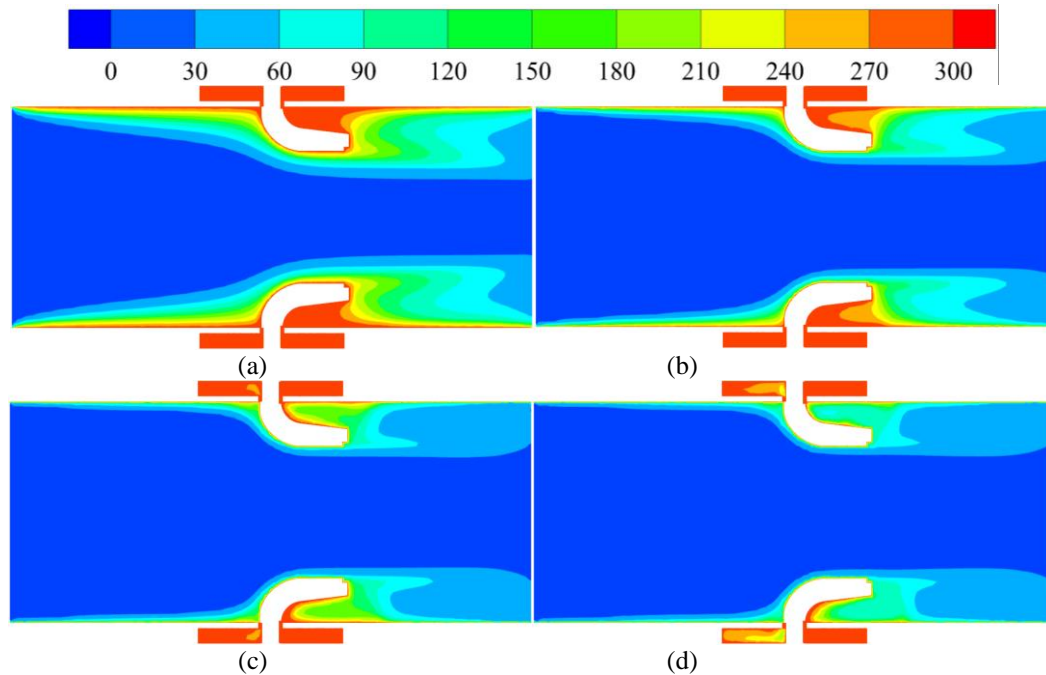


Figure 4 Temperature field of the cross-section in the flowmeter at 300°C
(a)10m³/h (b)100m³/h (c)500m³/h (d)1000m³/h

Figure 5 shows the cross-sectional temperature distribution of the fluid domain at various flow rates when the inner wall temperature is set to 500°C. As the flow rate increases, the internal heat transfer inside the nozzle flowmeter gradually decreases. During the process of increasing the flow rate from 10m³/h to 1000m³/h, the temperature stratification phenomenon in the internal temperature field of the flowmeter weakens. When the flow rate is 10m³/h, the heat transfer in the internal fluid domain of the nozzle flow meter is more pronounced. There is a smaller area of low-temperature region inside, and the high-temperature region extends towards the outlet of the flowmeter. When the flow rate is 1000m³/h, the heat transfer phenomenon inside the nozzle flowmeter is weaker, and the internal temperature stratification is mainly concentrated in the low temperature section.

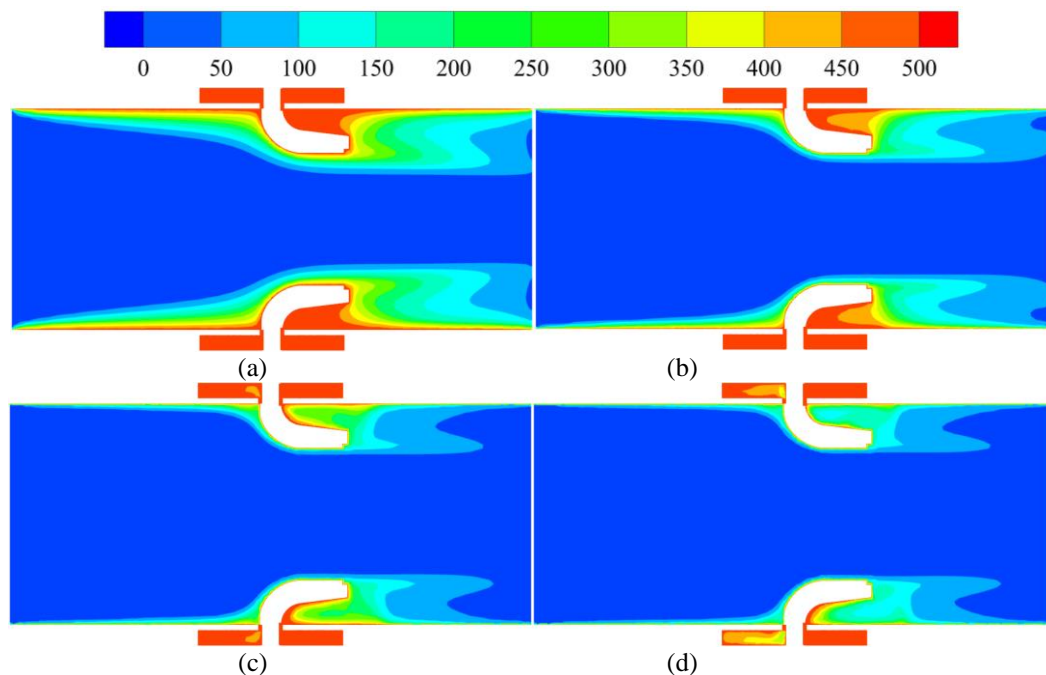


Figure 5 Temperature field of the cross-section in the flowmeter at 500°C
(a)10m³/h (b)100m³/h (c)500m³/h (d)1000m³/h

3.2 Pressure field

The Figure 6 shows the distribution of cross-sectional pressure in the fluid domain at various inner wall temperatures when the flow rate is $100 \text{ m}^3/\text{h}$. The internal pressure distribution of the flowmeter remains similar when the inner wall temperature is set at 50°C , 100°C , 300°C , 500°C , and 1000°C . During the process of increasing the inner wall temperature from 50°C to 1000°C , the pressure field inside the flowmeter fluid domain exhibits a distribution of gradually decreasing pressure from the inlet to the outlet of the flowmeter. A low pressure region with a pressure value of -3.9 Pa was found in the eight-slot nozzle. This indicates that the influence of the inner wall temperature of the flowmeter on the fluid domain is relatively small.

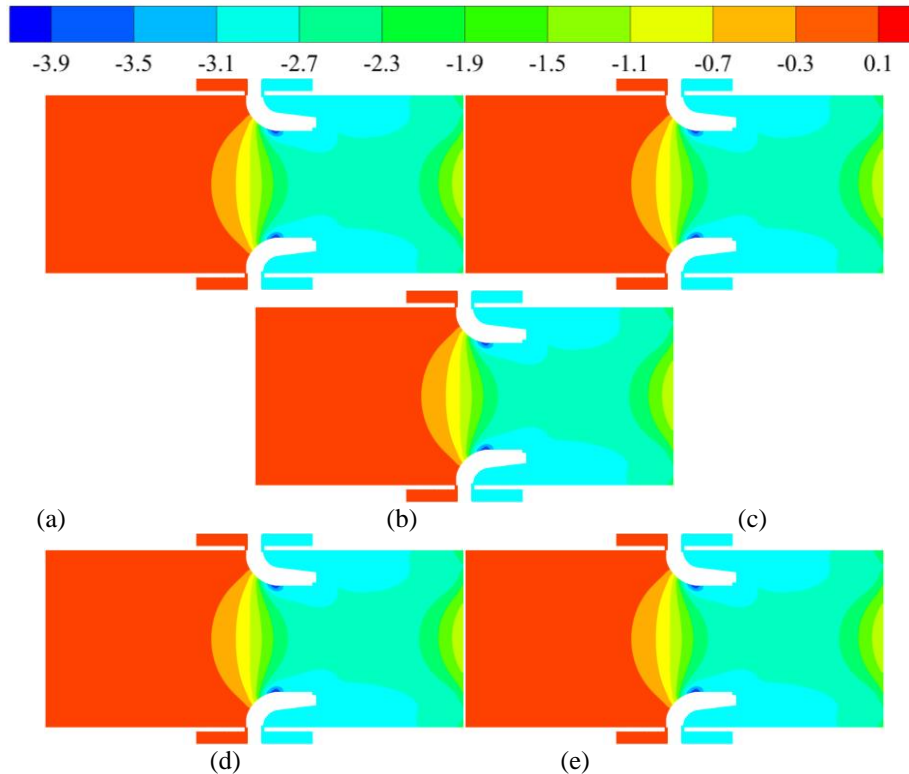


Figure 6 Pressure field of the cross-section in the flowmeter ($100 \text{ m}^3/\text{h}$)
(a) 50°C (b) 100°C (c) 300°C (d) 500°C (e) 700°C

The Figure 7 shows the distribution of cross-sectional pressure in the fluid domain at various inner wall temperatures when the flow rate is $500 \text{ m}^3/\text{h}$. The internal pressure distribution of the flowmeter remains similar when the inner wall temperature is set at 50°C , 100°C , 300°C , 500°C , and 1000°C . During the process of increasing the inner wall temperature from 50°C to 1000°C , the pressure field inside the flowmeter fluid domain exhibits a distribution of gradually decreasing pressure from the inlet to the outlet of the flowmeter. A low pressure region with a pressure value of -74 Pa was found in the eight-slot nozzle.

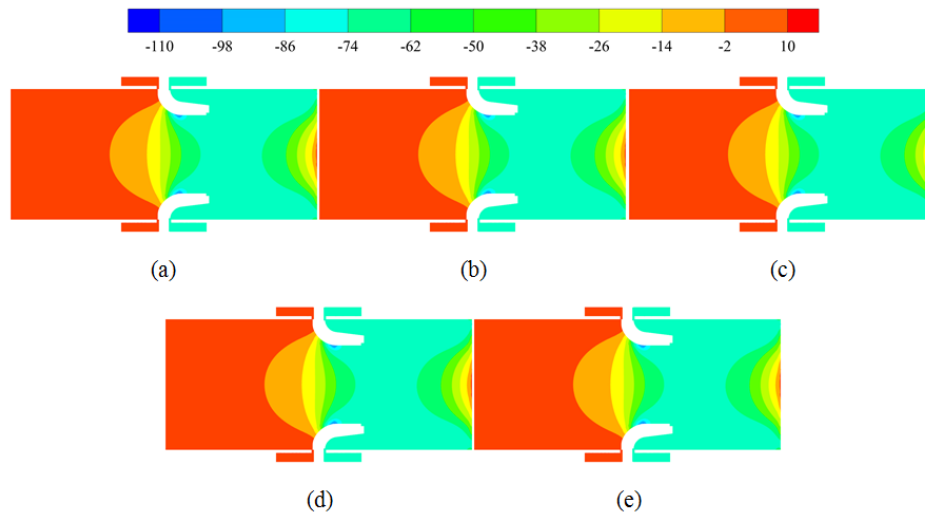


Figure 7 Pressure field of the cross-section in the flowmeter (500m³/h)
(a)50°C (b)100°C (c)300°C (d)500°C (e)700°C

3.3 Equivalent dynamic stress

The concept of equivalent dynamic stress is introduced based on the fourth strength theory, and the formula for equivalent dynamic stress σ_{eq} is

$$\sigma_{eq} = \sqrt{\frac{1}{2} \left[(\sigma_x - \sigma_y)^2 + (\sigma_y - \sigma_z)^2 + (\sigma_z - \sigma_x)^2 \right]} \quad (6)$$

In the formula, σ_x , σ_y and σ_z is the first, second, and third principal stress.

Figure 8 shows the distribution of dynamic stress in the flowmeter at a flow rate of 100 m³/h under various inner wall temperatures. The internal dynamic stress of the nozzle flowmeter is similar when the inner wall temperature is 50°C, 100°C, 300°C, 500°C and 1000°C. During the process of increasing the inner wall temperature from 50°C to 1000°C, the higher dynamic stress region inside the fluid domain of the flowmeter is consistently observed at the inlet and outlet of the eight slot nozzle, but the value of dynamic stress region remain relatively low, which is 2.31 Pa. This indicates that the inner wall temperature of the flowmeter has a small impact on the dynamic stress generated by the fluid inside the flowmeter.

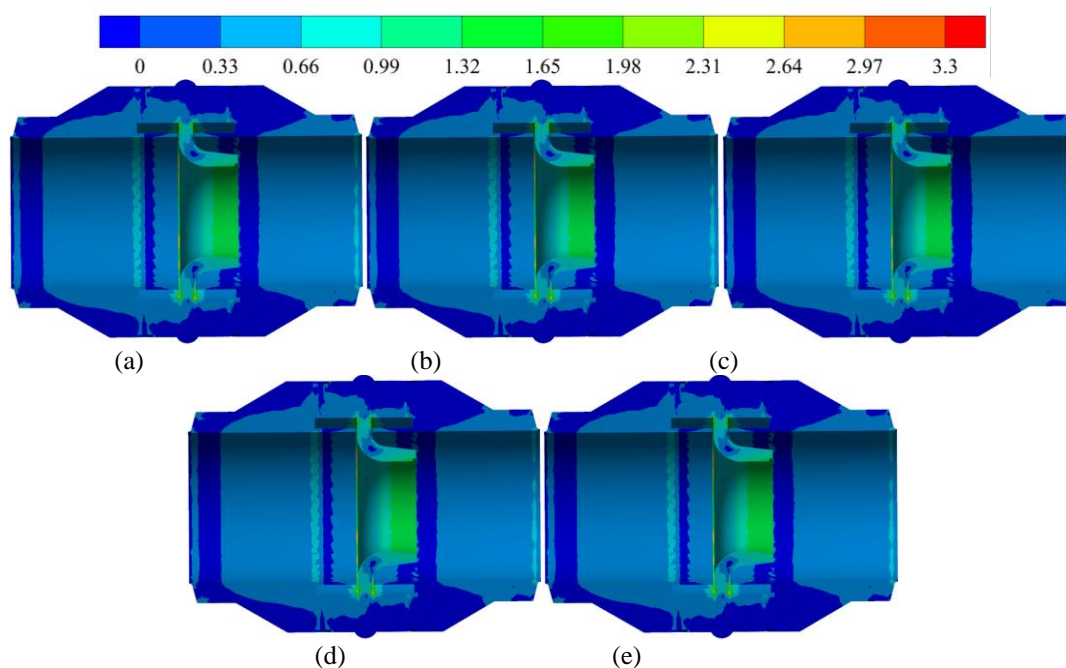


Figure 8 The cross-sectional dynamic stress in the flowmeter (100m³/h)
(a)50°C (b)100°C (c)300°C (d)500°C (e)700°C

Figure 9 shows the distribution of dynamic stress in the flowmeter at a flow rate of 500 m³/h under various inner wall temperatures. The internal dynamic stress of the nozzle flowmeter is similar when the inner wall temperature is 50°C, 100°C, 300°C, 500°C and 1000°C. During the process of increasing the inner wall temperature from 50°C to 1000°C, the higher dynamic stress region inside the fluid domain of the flowmeter is consistently observed at the inlet and outlet of the eight slot nozzle, but the value of dynamic stress region remain relatively low, which is 7 Pa. This indicates that the inner wall temperature of the flowmeter has a small impact on the dynamic stress generated by the fluid inside the flowmeter.

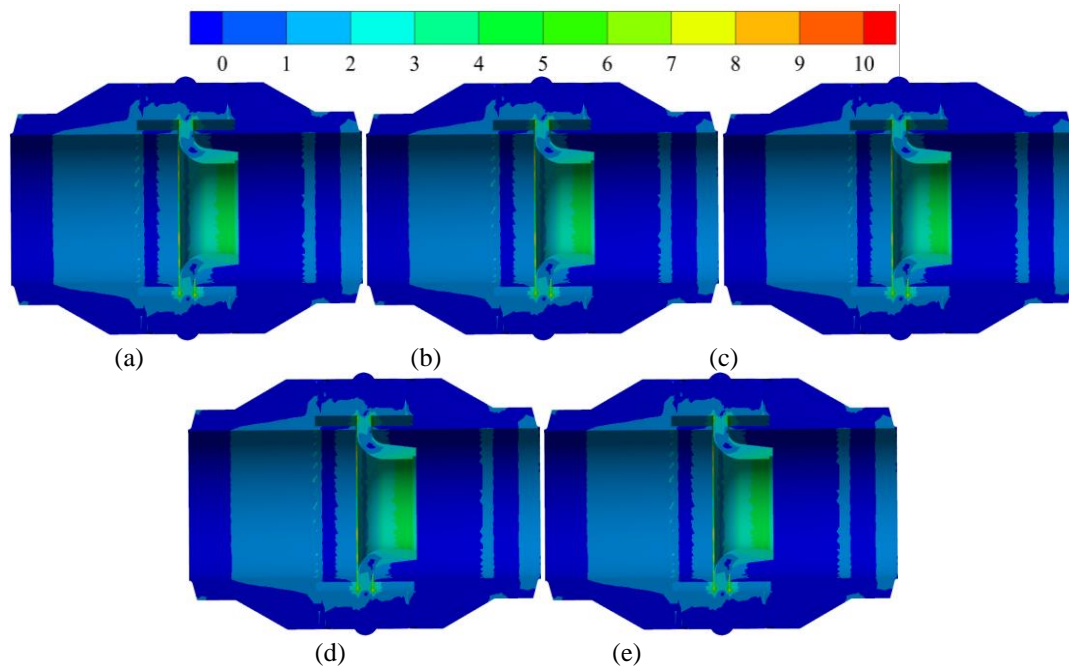


Figure 9 The cross-sectional dynamic stress in the flowmeter (500m³/h)
(a)50°C (b)100°C (c)300°C (d)500°C (e)700°C

3.4 Fluid-induced vibration deformation

The changes in the fluid domain of the flowmeter can cause deformation in the structural field of the flow rate meter, and this phenomenon is known as fluid-induced vibration. This paper is based on a single-phase fluid-solid coupling calculation method to analyze the fluid induced vibration deformation of nozzle flowmeter at different flow rate and internal wall temperature.

Figure 10 shows the distribution of fluid-induced vibration deformation inside the flowmeter under a flow rate of 100 m³/h at various inner wall temperature. It can be found that the fluid-induced vibration deformation in the fluid domain of the flowmeter remains similar at different inner wall temperatures of the nozzle flowmeter, ranging from 50°C to 1000°C. During the process of increasing the inner wall temperature from 50°C to 1000°C, the higher deformation region within the fluid domain of the flowmeter is observed at the inlet and outlet of the eight-slot nozzle, but the value is still relatively low, measuring 0.016 μm. This indicates that the inner wall temperature of the nozzle flowmeter has a small impact on the vibration deformation induced by the fluid.

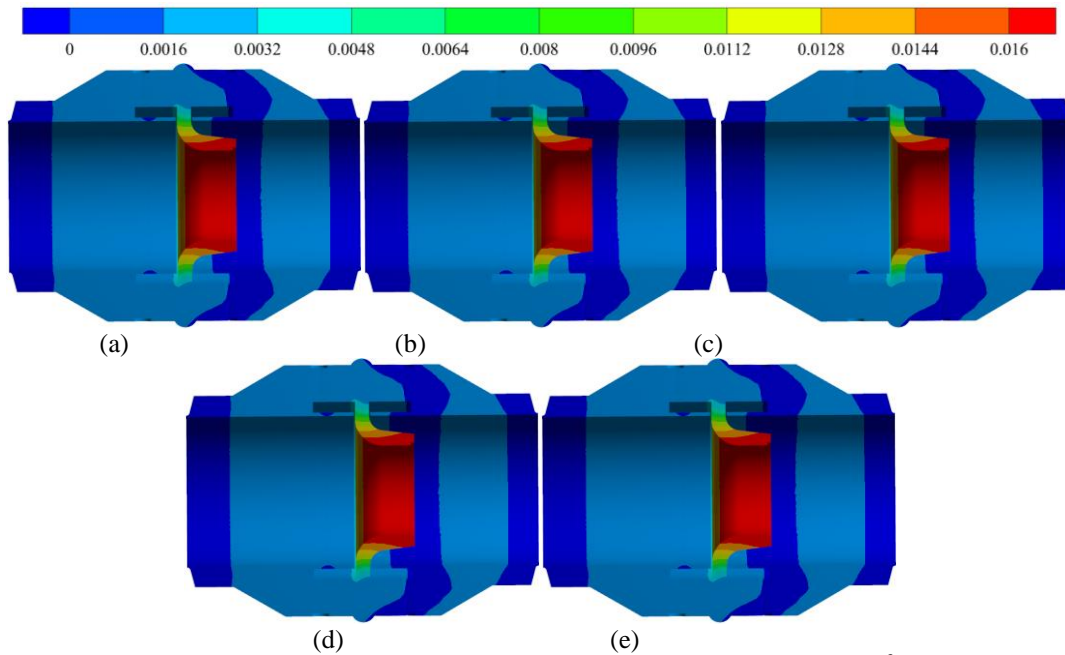


Figure 10 The cross-sectional thermal stress in the flowmeter ($100\text{m}^3/\text{h}$)
 (a) 50°C (b) 100°C (c) 300°C (d) 500°C (e) 700°C

Figure 11 shows the distribution of fluid-induced vibration deformation inside the flowmeter under a flow rate of $500\text{ m}^3/\text{h}$ at various inner wall temperature. It can be found that the fluid-induced vibration deformation in the fluid domain of the flowmeter remains similar at different inner wall temperature of the nozzle flowmeter, ranging from 50°C to 1000°C . During the process of increasing the inner wall temperature from 50°C to 1000°C , the higher deformation region in the fluid domain of the flowmeter is found at the inlet and outlet of the eight-slot nozzle, but the value is remain relatively low, measuring $0.46\text{ }\mu\text{m}$. This indicates that the inner wall temperature of the nozzle flowmeter has a relatively small impact on the vibration displacement induced by the fluid.

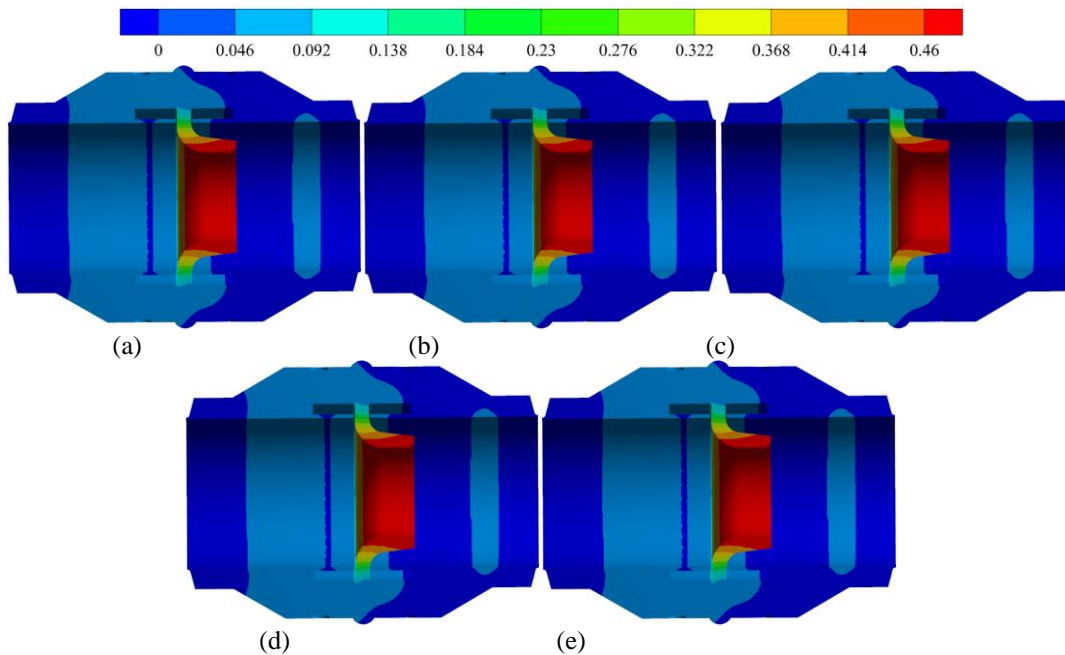


Figure 11 The cross-sectional thermal stress in the flowmeter ($500\text{m}^3/\text{h}$)
 (a) 50°C (b) 100°C (c) 300°C (d) 500°C (e) 700°C

IV. Conclusions

In this paper, a one-way fluid-structure interaction numerical simulation method was utilized to carry out numerical calculations for a nozzle flowmeter under different flow rates and different internal wall temperatures. It was found that under different internal wall temperatures, the internal heat transfer decreases gradually with increasing flow rate. The variation of the internal wall temperature has a relatively small effect on the internal pressure field, dynamic stress, and vibration deformation induced by the fluid.

ACKNOWLEDGEMENTS

The work was supported by the national college students' science and technology innovation project (No. 202211488028).

References

- [1]. Sheikh N, Singh S N, Veeravalli S V, et al. Effect of Reynolds number and boundary layer thickness on the performance of V-cone flowmeter using CFD[J]. Flow Measurement and Instrumentation, 2020, 73: 101728. (<https://doi.org/10.1016/j.flowmeasinst.2020.101728>)
- [2]. Sheikh N, Singh S N, Veeravalli S V, et al. Shape optimization of the cone body for the improved performance of the V-cone flowmeter: A numerical study[J]. Flow Measurement and Instrumentation, 2019, 66: 111-118. (<https://doi.org/10.1016/j.flowmeasinst.2019.02.001>)
- [3]. Perumal K, Krishnan J. A CFD study of the effect of venturi geometry on high pressure wet gas metering[J]. International Journal of Oil, Gas and Coal Technology, 2013, 6(5): 549-566. (<https://doi.org/10.1504/IJOGCT.2013.056101>)
- [4]. Enz S. Effect of asymmetric actuator and detector position on Coriolis flowmeter and measured phase shift[J]. Flow Measurement and Instrumentation, 2010, 21(4): 497-503. (<https://doi.org/10.1016/j.flowmeasinst.2010.07.003>)
- [5]. Huang T X, Ren J X, Zhang P. Fluid-structure interaction analysis of coriolis mass flowmeter[J]. International Journal of Modern Physics B, 2020, 34(14n16): 2040119. (<https://doi.org/10.1142/S0217979220401190>)
- [6]. Costa F O, Pope J G, Gillis K A. Modeling temperature effects on a Coriolis mass flowmeter[J]. Flow Measurement and Instrumentation, 2020, 76: 101811. (<https://doi.org/10.1016/j.flowmeasinst.2020.101811>)
- [7]. Shavrina E, Zeng Y, Khoo B C, et al. The Investigation of Gas Distribution Asymmetry Effect on Coriolis Flowmeter Accuracy at Multiphase Metering[J]. Sensors, 2022, 22(20): 7739. (<https://doi.org/10.3390/s22207739>)
- [8]. Prabu S V, Mascamani R, Balakrishnan K, et al. Effects of upstream pipe fittings on the performance of orifice and conical flowmeters[J]. Flow Measurement and Instrumentation, 1996, 7(1): 49-54. ([https://doi.org/10.1016/0955-5986\(96\)00001-5](https://doi.org/10.1016/0955-5986(96)00001-5))
- [9]. Singh V K, Tharakan T J. Numerical simulations for multi-hole orifice flow meter[J]. Flow Measurement and Instrumentation, 2015, 45: 375-383. (<https://doi.org/10.1016/j.flowmeasinst.2015.08.004>)
- [10]. Moosa M, Hekmat M H. Numerical investigation of turbulence characteristics and upstream disturbance of flow through standard and multi-hole orifice flowmeters[J]. Flow Measurement and Instrumentation, 2019, 65: 203-218. (<https://doi.org/10.1016/j.flowmeasinst.2019.01.002>)
- [11]. Rzasna M R, Czaplak-Nielacna B. Analysis of the influence of the Vortex Shedder shape on the metrological properties of the vortex flow meter[J]. Sensors, 2021, 21(14): 4697. (<https://doi.org/10.3390/s21144697>)
- [12]. Mohadikar K, Venugopal A, Agrawal A, et al. Improvement in the performance of the vortex flowmeter using contraction cone[J]. Measurement, 2017, 111: 316-332. (<https://doi.org/10.1016/j.measurement.2017.07.050>)
- [13]. Guo S, Zhang T, Sun L, et al. Blade shape optimization of liquid turbine flow sensor[J]. Transactions of Tianjin University, 2016, 22: 144-150. (<https://doi.org/10.1007/s12209-016-2685-z>)
- [14]. Guo S, Sun L, Zhang T, et al. Analysis of viscosity effect on turbine flowmeter performance based on experiments and CFD simulations[J]. Flow Measurement and Instrumentation, 2013, 34: 42-52. (<https://doi.org/10.1016/j.flowmeasinst.2013.07.016>)
- [15]. Zhang C L, Cui B L, Zhang Y L, et al. Experimental and numerical study on swirlmeter with different helix angles of swirler[J]. Transactions of the Institute of Measurement and Control, 2019, 41(11): 3103-3120. (<https://doi.org/10.1177/0142331218823859>)
- [16]. Cui B L, Zhang C L, Zhang Y L. Experimental and numerical studies on metrological characteristics of swirlmeters with different swirler helix angles in a gas-solid two-phase flow[J]. Flow measurement and instrumentation, 2020, 74: 101779. (<https://doi.org/10.1016/j.flowmeasinst.2020.101779>)
- [17]. Chen D, Cui B, Zhu Z. Numerical simulations for swirlmeter on flow fields and metrological performance[J]. Transactions of the Institute of Measurement and Control, 2018, 40(4): 1072-1081. (<https://doi.org/10.1177/0142331216673424>)
- [18]. Hollingshead C L, Johnson M C, Barfuss S L, et al. Discharge coefficient performance of Venturi, standard concentric orifice plate, V-cone and wedge flow meters at low Reynolds numbers[J]. Journal of Petroleum Science and Engineering, 2011, 78(3-4): 559-566. (<https://doi.org/10.1016/j.petrol.2011.08.008>)
- [19]. Düz H. Effect of conical angle on the hydraulic properties of orifice plate flows: A numerical approach[J]. Flow Measurement and Instrumentation, 2021, 81: 102026. (<https://doi.org/10.1016/j.flowmeasinst.2021.102026>)
- [20]. Zhang H, Guo C, Lin J. Effects of velocity profiles on measuring accuracy of transit-time ultrasonic flowmeter[J]. Applied Sciences, 2019, 9(8): 1648. (<https://doi.org/10.3390/app9081648>)
- [21]. Alaeddin M A, Hashemabadi S H, Mousavi S F. Numerical study on the effect of circumferential position of ultrasonic transducers on ultrasonic cross-correlation flowmeter performance under asymmetric air flow profile[J]. Ultrasonics, 2021, 115: 106479. (<https://doi.org/10.1016/j.ultras.2021.106479>)
- [22]. Min B, Logan B E. Continuous electricity generation from domestic wastewater and organic substrates in a flat plate microbial fuel cell[J]. Environmental science & technology, 2004, 38(21): 5809-5814. (<https://doi.org/10.1021/es0491026>)
- [23]. Yin J G, Li J. Discussion on site detection technology of steam flowmeter. Metrology & Measurement Technique, 2016, 43(1), 48 - 56.
- [24]. Oh S T, Park J J, Kim Y I, et al. Design of Multi Nozzles for a Portable Air Flow Meter using Numerical Simulation[J]. ASHRAE Transactions, 2019, 125.
- [25]. Wang Y, Yan Y, Zhou J, Li S. Flow Field Numerical Simulation and Pressure Tapping Location Optimization of Nozzle Flow Meter. Contemporary Chemical Industry, 2018, 47(10), 2161 - 2164, 2177.
- [26]. Zhang Y L, Tong L H, Xiao J J, et al. INFLUENCE OF WALL TEMPERATURE ON THERMAL EFFECT OF NOZZLE FLOWMETER[J]. Frontiers in Heat and Mass Transfer (FHMT), 2022, 18. (<http://dx.doi.org/10.5098/hmt.18.38>)

- [27]. Kim Y J, Yang J S, Kim B S. NUMERICAL STUDY ON THE IMPROVEMENT OF FOULING EFFECT ACCORDING TO THE RING SHAPE INSERTED INTO THE NOZZLE FLOWMETER[J]. *Journal of Computational Fluids Engineering*, 2018, 23(2).
- [28]. Zhang Y L, Tong L H, Yu T H, et al. HEAT FLOW DISTRIBUTION CHARACTERISTICS OF SOLID WALL OF NOZZLE FLOWMETER[J]. *Frontiers in Heat and Mass Transfer (FHMT)*, 2023, 20. (<http://dx.doi.org/10.5098/hmt.20.10>)
- [29]. Singh R K, Singh S N, Seshadri V. CFD prediction of the effects of the upstream elbow fittings on the performance of cone flowmeters. *Flow Measurement and Instrumentation*, 2010, 21(2), 88–97. (<https://doi.org/10.1016/j.flowmeasinst.2010.01.003>)
- [30]. Tong L H, Zheng S L, Zhang Y L, et al. Study on Thermal Effect of Nozzle Flowmeter Based on Fluid-Solid Coupling Method[J]. *Shock and Vibration*, 2021, 2021: 1-11. (<https://doi.org/10.1155/2021/7448439>)